Journal of The
Electrochemical Society

Estimating Heat Generation Rate of Cylindrical Lithium-Ion Batteries by a Transfer Function

To cite this article: Yizhan Xie *et al* 2025 *J. Electrochem. Soc.* **172** 080505

Journal of The Electrochemical Society, 2025 **172** 080505
1945-7111/2025/172(8)/080505/11/$40.00

Estimating Heat Generation Rate of Cylindrical Lithium-Ion Batteries by a Transfer Function

Yizhan Xie,[1] Xibin Lu,[1,2] Penxiao Bao,[3] Yiqing Li,[1] Zecheng Gan,[3] Dianxun Xiao,[1] Tong-Yi Zhang,[1,3,z] and Jiaqiang Huang[1,2,z]

[1]*Guangzhou Municipal Key Laboratory of Materials Informatics and Sustainable Energy and Environment Thrust, The Hong Kong University of Science and Technology (Guangzhou), Nansha, Guangzhou, 511400, Guangdong, People's Republic of China*
[2]*Academy of Interdisciplinary Studies, The Hong Kong University of Science and Technology, Clear Water Bay, Kowloon, 999077, Hong Kong, People's Republic of China*
[3]*Advanced Materials Thrust, The Hong Kong University of Science and Technology (Guangzhou), Nansha, Guangzhou, 511400, Guangdong, People's Republic of China*

Measuring the heat generation rate of batteries is essential for their thermal management. To acquire the heat generation rate, the calorimeters are costly, while model-based methods are relatively low-cost but suffer from demanding data and/or compromised accuracy. To circumvent the dilemma, we develop a novel method with better accuracy to estimate the heat generation rate using only a single-point temperature by solving the inverse problem of the heat-generation-rate-temperature transfer function. Validated across different battery formats (18650 and 3270 liFePO$_4$/graphite batteries), heat generation rates (from 0.5 C to 5 C), and ambient environments (oven, room, and silicone oil), we prove that this method accurately estimates the heat generation rate with either surface or internal temperatures measured by optical fiber sensors, offering ~56% less relative root mean squared error (RRMSE) than the conventional thermal network model. We also demonstrate another application of this approach: Using surface temperatures to derive the heat generation rate and then estimate internal temperatures, showing RRMSE below 3.2% at various discharge rates (0.5C-2C). This work not only facilitates the computation of the heat generation rate of batteries but also advances their thermal/thermodynamic studies together with battery sensors.
 [DOI: 10.1149/1945-7111/adf2e4]

Manuscript submitted May 19, 2025; revised manuscript received July 5, 2025. Published August 4, 2025.

Supplementary material for this article is available online

List of Symbols

Parameters

C	Specific heat capacity
dt	Time step
g	Volumetric heat generation rate distribution
$G(s)$	TF-MPFO from $\dot{Q}$ to temperature
h	Convection heat transfer coefficient
I	Current
k	Thermal conductivity
$K_d(x, y, z)$	Heat generation rate distribution
p_i	Additive inverse of $\mathscr{A}_{ij}(s)$ pole
P	SWAC period
$\dot{Q}$	Heat generation rate
s	Laplace variable
t	Time variable
t_{suff}	The time when the cooling period starts
T	Temperature
T_e	Excessed temperature
T_e^0	Initial value of T_e
T_{in}	Internal temperature
T_{steady}	The steady-state temperature
T_{surf}	Surface temperature
T_∞	Ambient air temperature
V	Voltage
V_{sys}	System domain
x	The first Cartesian coordinate
y	The second Cartesian coordinate
y_i	State variable of the i-th first-order subsystem
y_i^0	Initial value of y_i
y_{real}	Real value
y_{pred}	Predicted value
z	The third Cartesian coordinate
$\mathscr{A}$	A transfer function from heat generation rate to temperature
$\mathscr{A}_{ij}$	A component of $\mathscr{A}$
$\frac{\partial U}{\partial T}$	Entropic heat coefficient
∂V	Boundary surface
ρ	Mass density
$\dot{\mathscr{Q}}$	Laplace transformation of $\dot{Q}$
$\mathscr{T}_e$	Laplace transformation of T_e
$\mathbb{C}$	Complex number
$\mathbb{N}^+$	Positive integers
∇	Vector differential operator

Maintaining an optimal operational temperature range is critical for the safe and efficient operation of batteries. However, batteries inherently generate heat during operation, which presents a substantial risk of overheating and can trigger safety issues.[1–3] Therefore, an accurate estimation of the heat generation rate (denoted by $\dot{Q}$) for batteries is of paramount significance, as it directly informs the development of effective thermal management strategies to mitigate safety risks.[4,5] From another perspective, the $\dot{Q}$ fingerprints of batteries offer critical insights into their reaction mechanisms, namely, perceiving electrochemical processes via thermal signals.[6–13] Specifically, $\dot{Q}$ is associated with the formation of solid electrolyte interphases[6,13,14] and other parasitic reactions.[7,8] Therefore, the added values of acquiring heat generation of batteries are undoubtful.

To accurately measure $\dot{Q}$ in batteries, adiabatic[15–17] and isothermal calorimeters[18–20] were adopted to offer direct and precise results; however, their use is predominantly limited to specialized equipment, which is not only costly but also constrained to the dimension of the calorimeter chamber. To circumvent these limitations, models have been developed for estimating $\dot{Q}$ from easily measurable signals, such as temperature, current, and voltage. Prominent models include the electrochemical models,[21–26] neural network models,[27–30] and thermal network (TN) models.[31–39] These

[z]E-mail: mezhangt@hkust-gz.edu.cn; seejhuang@hkust-gz.edu.cn

models offer a way to establish the relationship between observable signals and $\dot{Q}$, thus providing a low-cost alternative to direct instrument-based methods.

Among the electrochemical models, the Bernardi equation is the most widely used due to its minimal parameter requirements and low computational load.[23,24] However, the difficulty of applying the Bernardi equation lies in acquiring thermodynamic variables such as equilibrium voltage and entropic heat coefficient.[24] In contrast to the Bernardi equation, neural network models rely on large amounts of data to overcome the necessity of physical variables and assumptions, which demonstrates successes under a few scenarios.[27–30] Nevertheless, neural network models are susceptible to overfitting and, therefore, require a substantial volume of data, limiting their practical applications.

Compared to the Bernardi equation and neural network models, thermal network models offer a physically intuitive representation by drawing an analogy to electric resistor-capacitor (RC) circuits. Namely, heat is driven from a higher temperature to a lower temperature through a medium that both resists heat flow and acts as a thermal capacitor to store thermal energy.[40] Owing to their intuitiveness and simplicity, thermal network models using a single set of resistor-capacitor (1-RC TN) are prevalently employed in the thermal modeling of batteries.[31–33] The 1-RC TN provides an advantage that only the two points (e.g., ambient and surface) of temperatures are needed,[31–33] whereas building a higher-order resistor-capacitor network necessitates additional temperature measurement points.[41] Anyway, heat generation and transfer in the battery are complicated three-dimensional (3D) physical processes, and simplifying these processes with a lumped thermal network inevitably introduces inaccuracies.[42]

Table I compares methods to estimate the heat generation rate of batteries, as discussed above. The need to develop a low-cost, high-accuracy, and easy-to-implement method is clear. Particularly, given our previous experience with thermal network models,[6,11,43] we hope to devise a method with better accuracy given a single temperature measurement point. To this end, we utilize the fundamental governing equations (such as the Fourier-Biot equation) in heat transfer and solving the inverse problem of $\dot{Q}$-temperature transfer function. This transfer function is rigorously derived and approximated for a specific heat transfer problem of batteries, which is composed of multiple parallel first-order systems (TF-MPFO). The performance of the as-developed model is examined in different battery formats (18650 and 3270 $LiFePO_4$/graphite batteries), current rates (from 0.5 C to 5 C), and ambient environments (oven, room, and silicone oil). In addition, we also show the versatility of our model in estimating the internal temperature via the surface temperature with excellent accuracy.

Methods

Transfer function from heat generation rate to temperature.—We consider a system (e.g., a battery) with an internal heat source, initially in thermal equilibrium with the surrounding air. The thermal dynamics are governed by the Fourier-Biot equation,[44] along with a natural convection boundary condition[45] and the corresponding initial conditions:

$$\begin{cases} \rho(x,y,z)C(x,y,z)\dfrac{\partial T(x,y,z,t)}{\partial t} = \nabla\cdot\nabla(k(x,y,z)T(x,y,z,t)) + g(x,y,z,t) \\ -k(x,y,z)\dfrac{\partial T(x,y,z,t)}{\partial \boldsymbol{n}}\bigg|_{\partial V_{sys}} = h(x,y,z)(T(x,y,z,t)|_{\partial V_{sys}} - T_\infty) \\ T(x,y,z,t=0) = T_\infty \end{cases} \quad [1]$$

where, $T(x, y, z, t)$ represents the temperature field; x, y, and z denote the Cartesian coordinates in three-dimensional space; t is the time variable; g represents the volumetric heat generation rate distribution; ∇ is the vector gradient operator. The material properties include mass density (ρ), specific heat capacity (C), and thermal conductivity (k). Let V_{sys} denotes the system domain, with ∂V being its boundary surface. $\frac{\partial T}{\partial n}|_{\partial V_{sys}}$ specifies the normal temperature gradient at the boundary. The boundary condition parameters involve the convection coefficient (h) and ambient temperature (T_∞).

For simplification, we define the excess temperature as

$$T_e(x,y,z,t) = T(x,y,z,t) - T_\infty \quad [2]$$

Substituting (2) into (1) transforms the system into

$$\begin{cases} \rho(x,y,z)C(x,y,z)\dfrac{\partial T_e(x,y,z,t)}{\partial t} = \nabla\cdot\nabla(k(x,y,z)T_e(x,y,z,t)) + g(x,y,z,t) \\ -k(x,y,z)\dfrac{\partial T_e(x,y,z,t)}{\partial \boldsymbol{n}}\bigg|_{\partial V_{sys}} = h(x,y,z)T_e(x,y,z,t)|_{\partial V_{sys}} \\ T_e(x,y,z,t=0) = 0 \end{cases} \quad [3]$$

We postulate that $g(x, y, z, t)$ can be decomposed into a spatial distribution function ($K_d(x, y, z)$) and the time-dependent heat generation rate ($\dot{Q}(t)$):

$$g(x,y,z,t) = K_d(x,y,z)\dot{Q}(t) \quad [4]$$

Accordingly, $\dot{Q}(t)$ can be obtained by integrating $g(x, y, z, t)$ over the spatial domain:

$$\dot{Q}(t) = \iiint_{V_{sys}} g(x,y,z,t)\,dxdydz \quad [5]$$

Applying the Laplace transform to (3) and (4) yields

$$\begin{cases} \rho(x,y,z)C(x,y,z)s\mathscr{T}_e(x,y,z,s) = \nabla\cdot\nabla(k(x,y,z)\mathscr{T}_e(x,y,z,s)) + K_d(x,y,z)\dot{\mathscr{Q}}(s) \\ -k(x,y,z)\dfrac{\partial \mathscr{T}_e(x,y,z,s)}{\partial \boldsymbol{n}}\bigg|_{\partial V} = h(x,y,z)\mathscr{T}_e(x,y,z,s)|_{\partial V} \end{cases} \quad [6]$$

where s is the Laplace variable; $\mathscr{T}_e(x, y, z, s)$ and $\dot{\mathscr{Q}}(s)$ are the Laplace transformation of $T_e(x, y, z, t)$ and $\dot{Q}(t)$, respectively.

Defining the transfer function $\left(\mathscr{A}(x,y,z,s) = \frac{\mathscr{T}_e(x,y,z,s)}{\dot{\mathscr{Q}}(s)}\right)$, (6) becomes

$$\begin{cases} \rho(x,y,z)C(x,y,z)s\mathscr{A}(x,y,z,s) = \nabla\cdot\nabla(k(x,y,z)\mathscr{A}(x,y,z,s)) + K_d(x,y,z) \\ -k(x,y,z)\dfrac{\partial \mathscr{A}(x,y,z,s)}{\partial \boldsymbol{n}}\bigg|_{\partial V} = h(x,y,z)\mathscr{A}(x,y,z,s)\,|_{\partial V} \end{cases} \quad [7]$$

Thus, the solution of (7), $\mathscr{A}(x, y, z, s)$ fully characterizes the linear response between $\dot{Q}$ and T_e. By omitting spatial coordinates for brevity, the input-output relation is simplified to

$$\frac{\mathscr{T}_e(s)}{\dot{\mathscr{Q}}(s)} = \mathscr{A}(s) \quad [8]$$

Transfer function simplification.—The exact form of $\mathscr{A}$ is generally complex due to the distributed nature of heat transfer.[46] To enable practical implementation, we apply the following simplifications.

Padé approximation.—Using a Padé approximant,[47,48] $\mathscr{A}$ is approximated as a strictly proper rational function (to ensure causality[49,50]):

Table I. Comparison of methods to estimate the heat generation rate of batteries.

	Calorimeter	Bernardi equation	Neural network	Thermal network	Our transfer function method
Cost	High	Low	Medium	Low	Low
Applicable cell size	Depending on the chamber	All size	All size	All size	All size
Parameter determination	Easy	Difficulty in accuracy	Relying on the amount of data	Medium	Medium
Temperature point number	Depending on the setup	/	/	Depending on the order of RC	1
Accuracy	High	Medium	Relying on the amount of data	Medium	High

$$\mathscr{A}(s) \approx \frac{a_0 + a_1 s + a_2 s^2 + \ldots + a_m s^{\mathrm{m}}}{1 + b_1 s + b_2 s^2 + \ldots + b_l s^l},\ l > \mathrm{m} \tag{9}$$

Partial fraction decomposition.—Performing partial fraction decomposition[51] on (9) yields a sum of partial fractions:

$$\mathscr{A}(s) \approx \sum_{i=1}^{n} \sum_{j=1}^{m_i} \mathscr{A}_{ij}(s),\ n,\ m_i \in \mathbb{N}^+,\ r_{ij},\ p_i \in \mathbb{C} \tag{10}$$

$$\mathscr{A}_{ij}(s) = \frac{r_{ij}}{(s + p_i)^j} \tag{11}$$

where, p_i (with $\mathrm{Re}(p_i) < 0$ for stability) are the additive inverse of the poles obtained by solving

$$1 + b_1(-p_i) + b_2(-p_i)^2 \quad + \ldots + \quad b_l(-p_i)^l = 0 \tag{12}$$

Experimental simplification.—To experimentally determine the dominant terms in $\mathscr{A}_{ij}(s)$, thermal characterization tests were conducted on a commercial 3270-type $LiFePO_4$/graphite (LFP/C) cylindrical battery (6 Ah capacity) under controlled conditions. Namely, the battery was placed in a 25 °C oven under the natural convection cooling condition, aligning with the boundary conditions assumed in section Transfer function from heat generation rate to temperature.

A square-wave alternating current (SWAC) of ±12 A with a 20-s period was applied for 2 hours, followed by a 2-hour rest period for cooling (Fig. 1a). This symmetric current profile cancels cumulative reversible heat through charge-discharge cycle averaging.[6,25] The internal temperature was monitored via a core fiber Bragg grating (FBG) sensor positioned 3.5 cm from the negative terminal. The FBG sensors were selected here due to their small size, chemical inertness, and electromagnetic immunity.[6,52] The working principal of FBG is illustrated in Supplementary Note 1. Meanwhile, $\dot{Q}$ was calculated per period as

$$\dot{Q}(t) = \frac{1}{P}\int_{(k-1)P}^{kP} IVdt,\ (k-1)P < t < kP,\ k = 1, 2, 3, \ldots \tag{13}$$

where P denotes the SWAC period.

The resultant temperature and $\dot{Q}$ are shown in Fig. 1b, where the temperature showed exponential decay during the cooling phase. Correspondingly, the cooling phase response of $\mathscr{A}_{ij}(s)$ after reaching a steady-state temperature (T_{steady}) is:

$$T_{ij}(t) = (T_{steady} - T_\infty)\sum_{k=1}^{j} \frac{(p_i(t - t_{suff}))^{k-1}}{(k-1)!}\exp(-p_i(t - t_{suff}) + T_\infty,\ t \geqslant t_{suff} \tag{14}$$

where t_{suff} marks the cooling start time. It is obvious that complex poles in (14) will introduce oscillatory behavior of temperature, which contradicts the observed exponential temperature decay (Fig. 1b), necessitating retention of only real positive poles ($p_i > 0$).

Further analysis of the time derivative of (14):

$$\frac{dT_{ij}(t)}{dt} = -(T_{steady} - T_\infty)p_i^j\frac{(t - t_{suff})^{j-1}\exp(-p_i(t - t_{suff})}{(j-1)!},\quad t \geqslant t_{suff},\ p_i > 0 \tag{15}$$

reveals that higher-order terms ($j \geqslant 2$) introduce sigmoid decay, inconsistent with experimental data. Consequently, the transfer function reduces to a sum of first-order systems:

$$\mathscr{A}(s) \approx G(s) = \sum_{i=1}^{n} \frac{r_i}{s + p_i},\ p_i > 0 \tag{16}$$

termed a multiple parallel first-order (TF-MPFO) model. Implementation with $n = 1$ achieved 0.18 °C root mean squared error against experimental data (Fig. 1b), validating the simplification. Specifically, the determination of n was based on an incremental strategy, namely, we began with $n = 1$ (the lowest order) and gradually increased the value only if the parameter identification results (e.g., accuracy) were proved inadequate. This approach ensures an optimal balance between model complexity and performance.

Notably, this TF-MPFO is rigorously derived and approximated for the heat transfer problem. It eliminates the requirement for dimensional reduction from 3-D thermal analysis to simplified 1D or lumped-parameter frameworks, which are commonly employed in conventional thermal network models.[31–37,41,53] This fundamental characteristic enables our methodology to operate with fewer assumptions while maintaining enhanced robustness across diverse operational scenarios.

From a single-point temperature to the heat generation rate.—With this specially simplified TF-MPFO, we propose a method called the inverse transfer function (Inv-TF) method to deduce $\dot{Q}(t)$ from T_e inversely. The methodology proceeds as follows.

First, (16) is converted into continuous state-space equations:

$$\frac{dy_i(t)}{dt} = -p_i y_i(t) + r_i\dot{Q}(t),\ i = 1, 2, \ldots, n \tag{17}$$

$$T_e(t) = y_1(t) + y_2(t) + \ldots + y_n(t) \tag{18}$$

where y_i represents the state variable of the i-th first-order subsystem.

Next, (17) is discretized using a fixed time step (dt). Let X^j denote the value of the variable ($X(t)$) at discrete time ($t = jdt$). Solving (17) and (18) analytically yields

$$y_i^j = A_i y_i^{j-1} + B_i\dot{Q}^{j-1},\ i = 1, 2, \ldots, n \tag{19}$$

$$T_e^j = y_1^j + y_2^j + \ldots + y_n^j \tag{20}$$

where,

$$A_i = \exp(-p_i dt); B_i = \frac{r_i}{p_i}(1 - A_i),\quad i = 1, 2, \ldots, n \tag{21}$$

By rearranging (19) and (20),

$$\begin{bmatrix} 1 & 0 & \cdots & 0 & -B_1 \\ 0 & 1 & \cdots & 0 & -B_2 \\ \vdots & \vdots & \ddots & \vdots & \vdots \\ 0 & 0 & \cdots & 1 & -B_n \\ 1 & 1 & \cdots & 1 & 0 \end{bmatrix}\begin{bmatrix} y_1^j \\ y_2^j \\ \vdots \\ y_n^j \\ \dot{Q}^{j-1} \end{bmatrix} = \begin{bmatrix} A_1 & 0 & \cdots & 0 & 0 \\ 0 & A_2 & \cdots & 0 & 0 \\ \vdots & \vdots & \ddots & \vdots & \vdots \\ 0 & 0 & \cdots & A_n & 0 \\ 0 & 0 & \cdots & 0 & 0 \end{bmatrix}\begin{bmatrix} y_1^{j-1} \\ y_2^{j-1} \\ \vdots \\ y_n^{j-1} \\ \dot{Q}^{j-2} \end{bmatrix} + \begin{bmatrix} 0 \\ 0 \\ \vdots \\ 0 \\ 1 \end{bmatrix} T_e^j \tag{22}$$

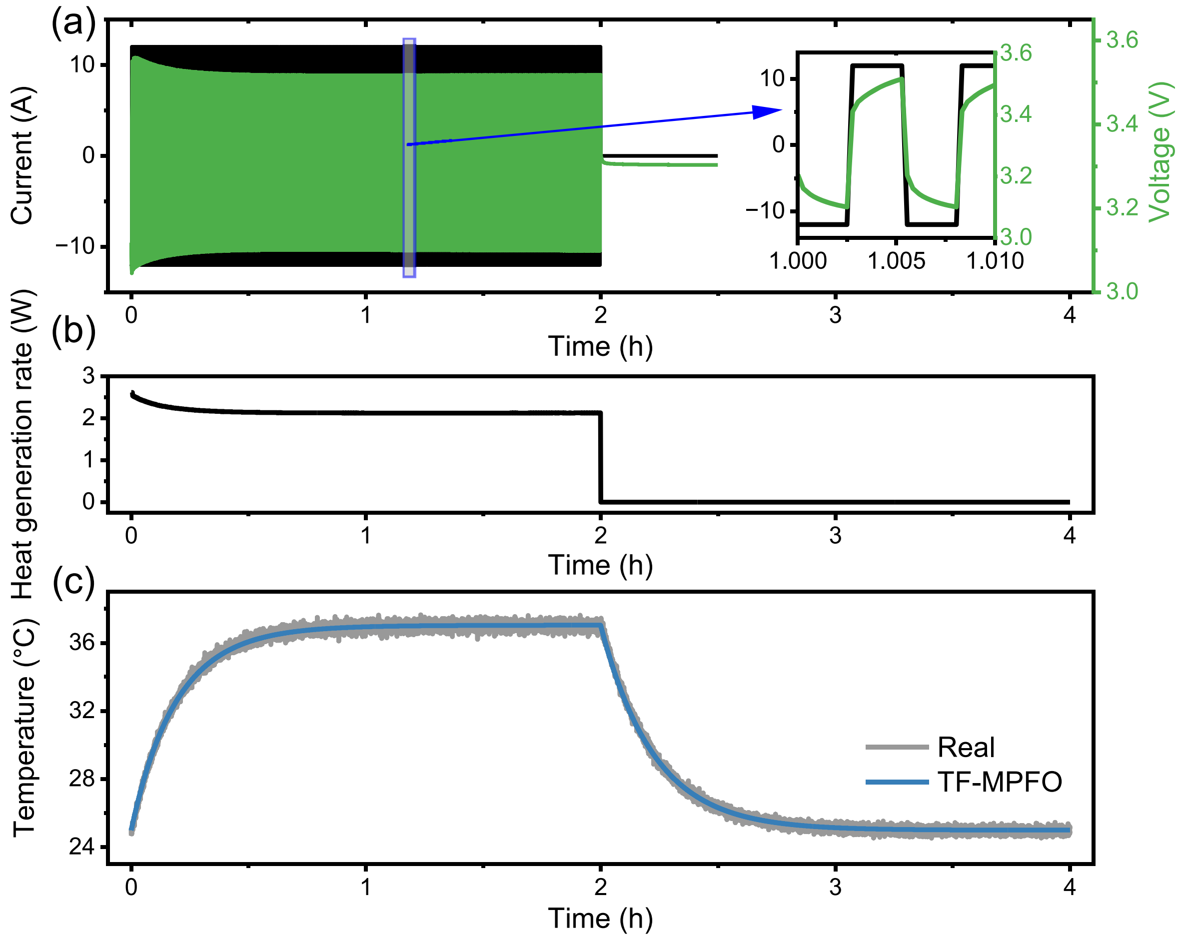

Figure 1. SWAC results of a 3270 LFP/C battery: (a) Current and voltage, (b) Heat generation rate, and (c) Internal temperature.

Solving $[y_1^j, y_2^j, \ldots, y_n^j, \dot{Q}^{j-1}]^T$ from (22) provides the iterative formula:

$$\begin{bmatrix} y_1^j \\ y_2^j \\ \vdots \\ y_n^j \\ \dot{Q}^{j-1} \end{bmatrix} = \begin{bmatrix} 1 & 0 & \cdots & 0 & -B_1 \\ 0 & 1 & \cdots & 0 & -B_2 \\ \vdots & \vdots & \ddots & \vdots & \vdots \\ 0 & 0 & \cdots & 1 & -B_n \\ 1 & 1 & \cdots & 1 & 0 \end{bmatrix}^{-1} \times \left\{ \begin{bmatrix} A_1 & 0 & \cdots & 0 & 0 \\ 0 & A_2 & \cdots & 0 & 0 \\ \vdots & \vdots & \ddots & \vdots & \vdots \\ 0 & 0 & \cdots & A_n & 0 \\ 0 & 0 & \cdots & 0 & 0 \end{bmatrix} \begin{bmatrix} y_1^{j-1} \\ y_2^{j-1} \\ \vdots \\ y_n^{j-1} \\ \dot{Q}^{j-2} \end{bmatrix} + \begin{bmatrix} 0 \\ 0 \\ \vdots \\ 0 \\ 1 \end{bmatrix} T_e^j \right\} \quad [23]$$

Lastly, considering the initial value of y_i and T_e, they are set to 0, that is

$$y_i^0 = 0,\ T_e^0 = 0 \quad [24]$$

This assumption reflects that the system starts in thermal equilibrium with the surrounding air.

In summary, the method procedure is illustrated in Fig. 2. Using this method, $\dot{Q}$ of a battery can be determined by using a single-point temperature measurement.

Results

Experimental setup.—FBG sensors were strategically positioned to measure both surface and internal temperatures at 1 Hz sampling frequency. Particularly, the measurements of internal temperatures were achieved by embedding sensors into a central void through the battery's positive terminal cover.

The FBG insertion was conducted in a dry room (Dew point: −55 °C) and involved 5 key steps: (1) Full discharge of the battery to ensure safety during modification; (2) Precision drilling of a 1-mm diameter access hole at the positive terminal's center; (3) Sensor insertion through the hole using a guidance needle for proper positioning; (4) Epoxy resin encapsulation to seal the entry point and ensure the air-tightness; (5) Curing and post-installation quality checks. Supplementary Fig. 2(a) illustrates the modified 3270 battery following successful sensor integration.

To quantify the sensor insertion's effects on the battery, electrochemical impedance spectroscopy tests were performed pre- and post-modification. As shown in Supplementary Fig. 2(b), the Nyquist plots exhibit negligible deviation between the pristine and modified batteries, confirming that the integration process did not affect the electrochemical behavior.

Additionally, to evaluate method accuracy, the relative root mean square error (RRMSE) is employed:

$$\mathrm{RRMSE} = \frac{\sqrt{(y_{real} - y_{pred})^2/N}}{\max(y_{real}) - \min(y_{real})} \quad [25]$$

where, y_{real} and y_{pred} represents the real and the predicted values, respectively, N is the sample count. This normalized metric enables

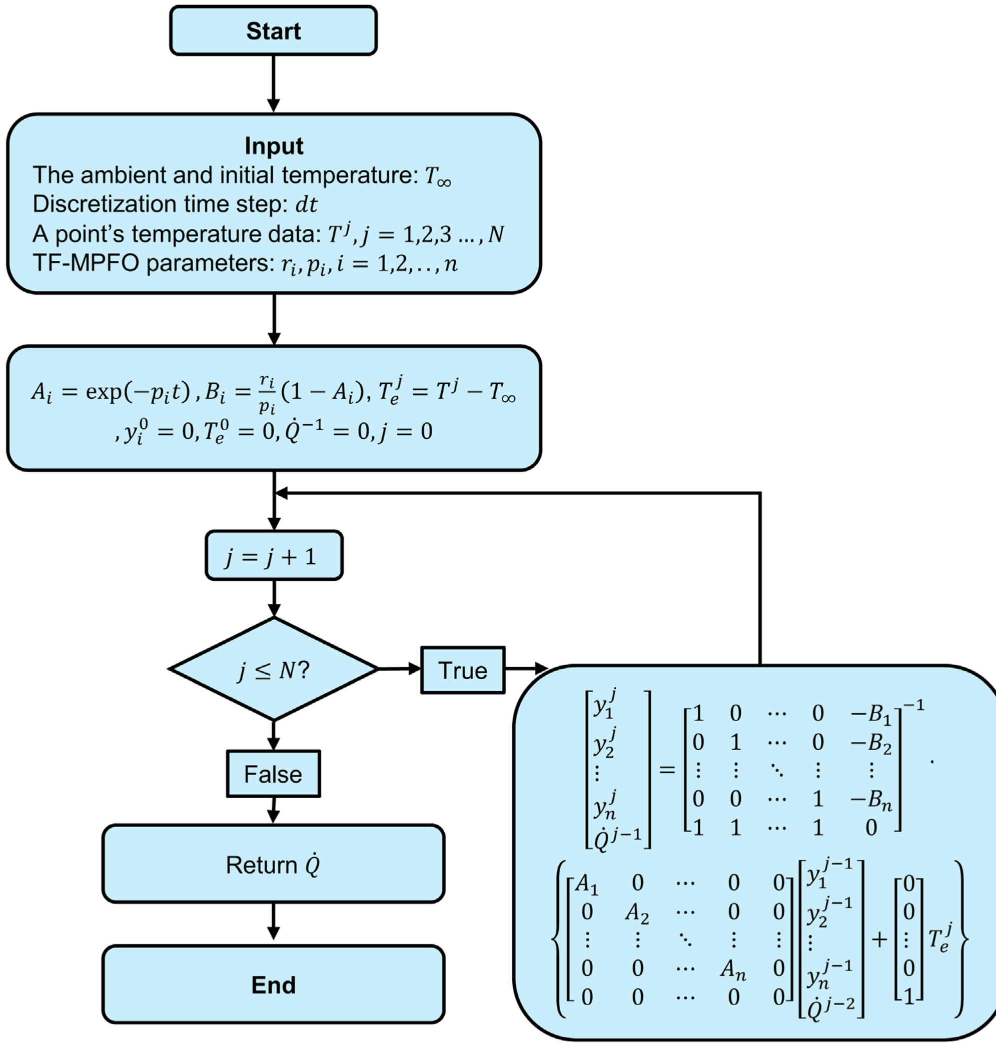

Figure 2. Procedure for Inv-TF method.

cross-condition comparison by accounting for measurement range variations.

Heat generation rate estimation.—*Results under the thermostatic oven condition.*—In this experimental configuration, the batteries were housed within a thermostatic oven maintained at 25 °C. To examine whether the location of the temperature sensor will influence the results, temperature measurements were recorded at six spatially distinct positions: Three axial locations within the battery's internal cavity (top, middle, bottom) and three corresponding points on its external surface. The axial positions were defined at heights of 5 cm (top), 3.5 cm (middle), and 2 cm (bottom) relative to the negative terminal cover. As shown in Supplementary Fig. 3, temperature profiles during a 1 C constant-current discharge exhibited minimal spatial variation along the vertical axis for both internal and surface measurements. Given this observed thermal uniformity, subsequent $\dot{Q}$ estimations were simplified by adopting the mid-height internal temperature (T_{in}) and surface temperature (T_{surf}) as representative thermal indicators.

Figure 3 presents the $\dot{Q}$ estimation results for the 3270 battery using the Inv-TF method during a multiple SWAC (MSWAC) test. As shown in Fig. 3a, the MSWAC protocol comprised four sequential 0.5-hour SWAC tests with current magnitudes of 1 C, 2 C, 1 C, and 0.5 C, each with a 20-s period. To mitigate noise effects, raw temperature data were smoothed using piecewise third-order polynomial functions prior to analysis, as shown in Fig. 3b.

As demonstrated in Fig. 3c, the Inv-TF method accurately reconstructed the $\dot{Q}$ profile using both T_{in} and T_{surf}, yielding low RRMSE of 1.19% and 1.89%, respectively. The marginally higher error for T_{surf}-based estimation may be attributed to its sensitivity to spatiotemporal heat dissipation variations.[54]

To validate the method under high-rate conditions, high-rate MSWAC tests were conducted for both 3270 and 18650 LFP/C batteries. While retaining the protocol structure from Fig. 3a, current magnitudes were elevated to 2 C/4 C/2 C/1 C for the 3270 and 2.5 C/5 C/2.5 C/1.5 C for the 18650 (Figs. 4a and 4b). As shown in Fig. 4c, the 3270 battery exhibited increased RRMSE values of 1.38% (T_{in}) and 3.19% (T_{surf}) compared to low-rate results (1.19% and 1.89% in Fig. 3c). This performance degradation aligns with intensified reaction non-uniformity at elevated currents, which induces dynamic $\dot{Q}$ distributions that violate the static assumption in (4).[55] Nonetheless, we demonstrate that even at 4 C conditions in Figs. 4a and 4b, the absolute error is limited to less than 0.5 W (~7% of the average heat generation rate of 7.4 W), indicating that the violation does not critically compromise the method's operational viability. More importantly, the performance degradation is smaller with T_{in} (0.19%) than that with T_{surf} (1.30%) on the whole, underscoring the importance of measuring internal temperatures. On the other hand, the 18650 battery demonstrated lower RRMSEs (1.86% and 2.09% for T_{in} and T_{surf}, respectively) than that of 3270 cells (1.38% and 3.19%), probably because the smaller dimensions mitigate spatial $\dot{Q}$ distribution variability.

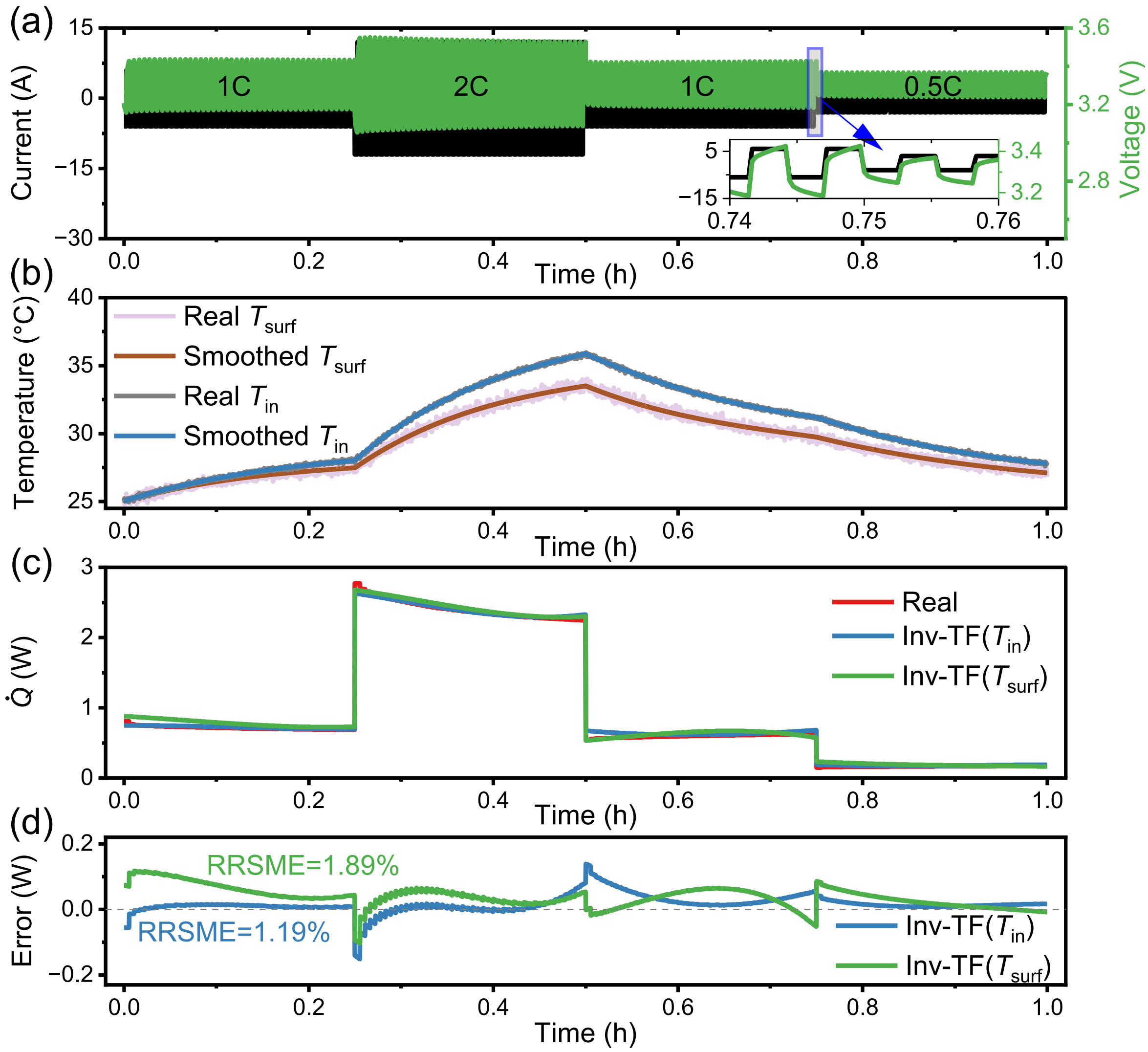

Figure 3. $\dot{Q}$ estimation results of a 3270 battery: (a) MSWAC current profile; (b) Smoothed temperatures; (c) $\dot{Q}$ estimation; (d) Error.

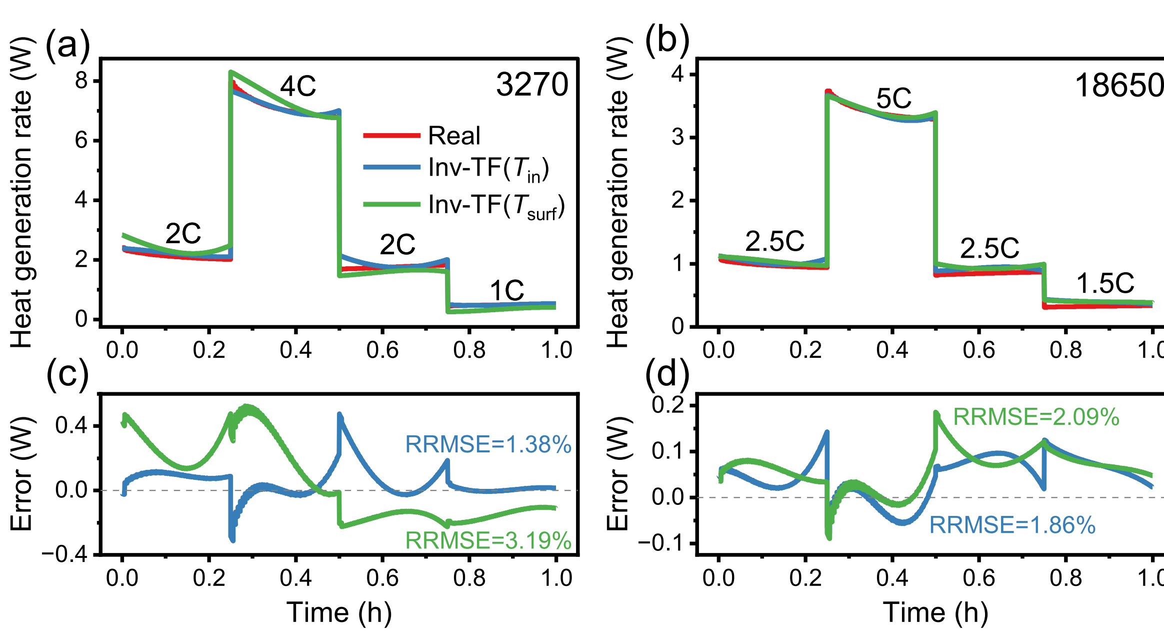

Figure 4. High-rate $\dot{Q}$ estimation and error analyses: (a,c) 3270 battery; (b,d) 18650 battery.

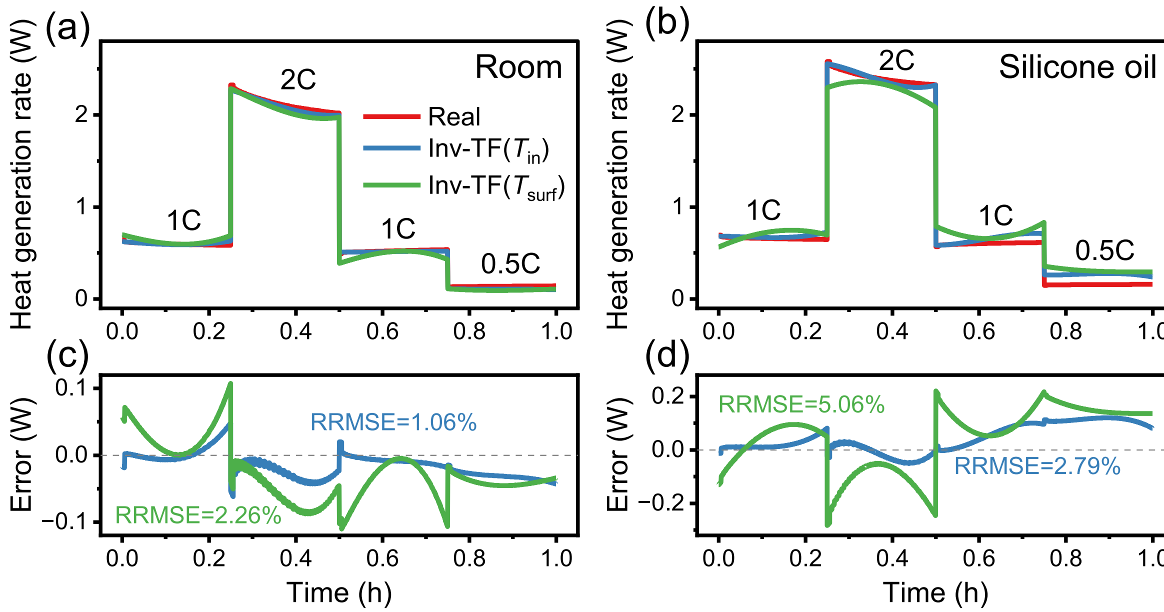

Figure 5. $\dot{Q}$ estimation under different environments: (a) Room; (b) Silicone oil.

Table II. RRMSE Comparison of Inv-TF and TN method.

Method	MSWC 3270 (Oven)	High-rate MSWC 3270 (Oven)	High-rate MSWC 18650 (Oven)	MSWC 3270 (Room)	MSWC 3270 (Silicone oil)	Average
Inv-TF (T_{in})	1.19%	1.38%	1.86%	1.06%	2.79%	1.66%
Inv-TF (T_{surf})	1.89%	3.19%	2.09%	2.26%	5.06%	2.90%
Thermal network	1.82%	2.52%	2.43%	4.83%	7.27%	3.75%

Furthermore, it is noted that the theoretical foundation of our approach, derived from core heat transfer principles and boundary conditions, is fundamentally applicable to any battery geometry, including pouch cells. To explicitly demonstrate this, we applied this method to estimate the heat generation rate of a 15 Ah LFP/C pouch cell using a surface temperature measurement, achieving good accuracy of 2.48% RRMSE, as shown in the Supplementary Fig. 4.

Validation in different ambient environments.—To assess robustness across operating conditions, the method was validated using the MSWAC test under distinct ambient environments. A 3270 battery was tested in two configurations: (1) exposed to ambient air in a room-temperature setting, representing typical operational conditions; and (2) submerged in silicone oil within a 25 °C thermostatic oven, simulating thermal management systems designed to optimize heat dissipation.[56–58]

The $\dot{Q}$ estimation results for both conditions are shown in Fig. 5. As shown in Fig. 5, $\dot{Q}$ estimation in air achieved RRMSE values of 1.06% (T_{in}) and 2.26% (T_{surf}), demonstrating reliable performance. Conversely, silicone oil immersion yielded higher errors (2.79% and 5.06% for T_{in} and T_{surf}, respectively), primarily due to an expanded interfacial region for the battery-silicone system compared to the air-only condition. The increased interfacial region amplifies spatio-temporal variations in convective heat transfer dynamics,[59] which contravenes the model's foundational assumption of time-invariant natural convection parameters, as indicated in (1). Consequently, the violation of this assumption—more pronounced under silicone oil immersion due to the larger interfacial region—induces systematic underestimation of transient thermal behavior. To improve accuracy, one possible future solution involves refining the TF-MPFO parameterization methodology, specifically by incorporating characteristics of complex interfacial heat transfer. Notably, under any conditions (room, air, or silicon oil), the model always performs better with T_{in}, showcasing the performance enhancement from the internal measurement.

Comparison with the thermal network model.—Furthermore, we conducted a performance comparison between the proposed Inv-TF method and the thermal network model[6,60] across the previous five experimental configurations. The detailed implementation of the thermal network model is described in Supplementary Note 2. As summarized in Table II, the Inv-TF method relying on T_{in} demonstrated better accuracy than the thermal network model across all conditions. Note that the thermal network model used 2 temperature points including both T_{in} and T_{surf}, while the as-developed Inv-TF method only needs a single-point temperature (either T_{in} or T_{surf}), highlighting the advance of our method. On average, the T_{in}- and T_{surf}-based Inv-TF method achieved lower RRMSEs of 1.66% and 2.90%, respectively, than that of the thermal network method (3.75%), offering improvements of 56% and 23%, respectively.

This performance gap likely originates from structural differences between the methodologies. The thermal network method employs a lumped-parameter modeling framework, which oversimplifies thermal dynamics by neglecting spatial temperature gradients—a critical limitation in geometrically complex systems such as batteries.[61] In contrast, the Inv-TF method implicitly accounts for distributed thermal behavior, as indicated in (1), enabling more precise estimation under dynamic operating conditions.

Internal temperature estimation.—The T_{in} is a crucial parameter for battery thermal management, requiring the implementation of

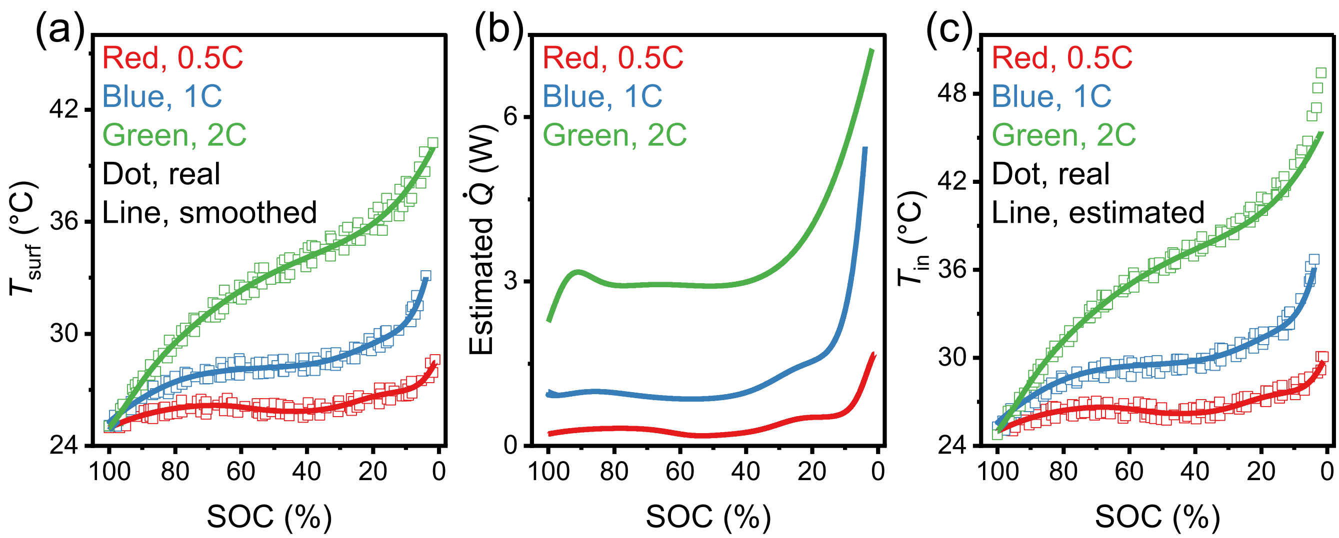

Figure 6. Internal temperature estimation for the 3270 LFP/C battery: (a) Measured T_{surf}; (b) Estimated $\dot{Q}$; (c) Measured and estimated T_{in}.

embedded sensors inside the battery.[6,62,63] However, in the short term, internal sensors are not available in commercial battery products. Here, our method could provide a framework for T_{in} estimation. The process begins by utilizing T_{surf} to estimate $\dot{Q}$ by the Inv-TF method, which is subsequently used to predict T_{in} by the TF-MPFO model. A critical preliminary step of this approach involves determining the parameters of the two TF-MPFOs for T_{in} and T_{surf}. All these parameters are identified through the SWAC experiment, as illustrated in Fig. 1. Additionally, to minimize noise interference, raw T_{surf} data undergoes smoothing prior to $\dot{Q}$ estimation. The derived $\dot{Q}$ values are then used to compute T_{in} via (19) and (20).

As shown in Fig. 6, the estimated T_{in} curves for the 3270 lFP/C battery maintain strong agreement with the real measurements, with notable deviations at low state of charge levels. This discrepancy likely stems from increased current distribution heterogeneity at a low state of charge (SOC), which induces localized $\dot{Q}$ fluctuations.[64] These fluctuations violate the fixed $\dot{Q}$ distribution assumption underlying our model, thereby introducing errors in low-SOC regimes. Overall, the RRMSE values for T_{in} estimation at 0.5 C, 1 C, and 2 C rates are 3.13%, 2.05%, and 2.45%, respectively. The slightly elevated RRMSE at 0.5 C likely arises from the narrower temperature range observed experimentally at this rate. Since RRMSE normalizes errors by the measurement range, reduced thermal dynamics at lower discharge rates amplify the relative error metric. In summary, the method achieves all RRMSE values below 3.2% at different rates. This metric confirms the method's remarkable accuracy in T_{in} estimation.

Notably, the estimated $\dot{Q}$ profiles in Fig. 6b exhibit characteristic peaks and valleys, consistent with entropy-driven thermal behavior in LFP/C batteries.[65] These "peaks and valleys" features arise directly from the entropy-driven reversible heat component ($\dot{Q}_{rev}$) of $\dot{Q}$ of the LFP/C chemistry and its variation with state of charge (SOC). In the mid-SOC range during discharge, the $\dot{Q}_{rev}$ is endothermic (heat absorption), creating the valleys in the total $\dot{Q}$. Conversely, at very low and high SOC, the $\dot{Q}_{rev}$ behaves exothermic (heat release). This exothermic heat release produces the observed peaks. This consistency implies the Inv-TF method's capacity to capture fundamental heat generation mechanisms.

While there may be some concerns about the practical feasibility of our T_{in} estimation framework—particularly regarding sensor intrusiveness and implementation cost. For the intrusiveness problem, our data confirms minimal intrusion: Supplementary Fig. 2(b) shows negligible deviation in Nyquist plots between pristine and modified cells, verifying preserved electrochemical behavior post-integration, with long-term stability further supported by prior work.[6] While for cost problems, we propose calibrating the $T_{surf} - T_{in}$ relationship using a small batch of sensor-instrumented batteries, then applying this correlation to sensor-free batteries from the same production batch. This strategy enables accurate internal temperature estimation while eliminating the need for pervasive sensor deployment, thereby enhancing commercial feasibility by reducing unit costs.

Conclusions

We developed a transfer-function-based method to estimate the heat generation rate ($\dot{Q}$) in cylindrical batterie using single-point temperature measurements. To validate its accuracy, we rigorously compared our approach with the traditional thermal network method across diverse experimental conditions, including 18650 and 3270 LFP/C batteries under varying thermal environments (oven, room, and silicone oil), heat generation rates (from 0.5 C to 5 C). By merely utilizing T_{in}, our method achieves significantly higher accuracy, yielding an average RRMSE of 1.66% for $\dot{Q}$ estimation in five different experimental configurations. Notably, the average accuracy of our method outperforms the thermal network model by 56%, even though the thermal network model utilized both T_{in} and T_{surf}. Furthermore, we demonstrate the method's capability to infer internal temperature from surface temperature, validated experimentally on 3270 LFP/C batteries with RRMSEs below 3.2% across multiple discharge rates (0.5C-2C).

Key advantages of our method include: (1) More easy-to-implement by a single-sensor temperature monitoring, (2) Robust with reduced reliance on assumptions inherent to conventional approaches (e.g., avoiding 3D-to−1D geometric simplifications), and (3) Dual functionality for both $\dot{Q}$ and T_{in} estimation.

However, our method also encounters several challenges. Firstly, data smoothing is required to eliminate noise inference. Secondly, the performance of the TF-MPFO method does show uncertainty; for instance, the T_{surf}-based estimation was less accurate, underscoring the importance of internal sensors. Overall, we believe our method is more versatile and robust to a wider array of complex scenarios, providing critical insights into battery thermal management research and applications.

Acknowledgments

The authors express gratitude for the financial support provided by the National Key R&D Program of China (No.

2023YFB2503600). This work was also supported by research grants from the National Natural Science Foundation of China (Nos. 52207230 and 92372109), and the Hong Kong University of Science and Technology (Guangzhou) startup grants (Nos. G0101000062 and G0101000099). Additionally, this research received funding from the Guangzhou-HKUST (GZ) Joint Funding Program (Nos. 2023A03J0003 and 2023A03J0103). The authors acknowledge the Materials Characterization and Preparation Facility (MCPF) at The Hong Kong University of Science and Technology (Guangzhou) for its experimental support. We acknowledge the facility, and service support from the Laboratory for Brilliant Energy Science and Technology (BEST Lab) at the Hong Kong University of Science and Technology (Guangzhou). The authors are also indebted to Prof. Jean-Marie Tarascon for his professional advice on this paper, which played a key role in enhancing its academic quality. During the preparation of this work, the authors used DeepSeek to improve language and readability. After using this tool service, the authors reviewed and edited the content as needed and took full responsibility for the content of the publication.

CRediT Authorship Contribution Statement

J. Huang and T.-Y. Zhang managed the project and guided the research. Y. Xie proposed the idea, conducted simulations, and performed data analysis. X. Lu and Y. Li designed and conducted the experiments. Y. Xie, P. Bao, T.-Y. Zhang, D. Xiao, and Z. Gan established the theory. Y. Xie and J. Huang wrote the paper with contributions from all authors.

Declaration of Competing Interests

The authors declare no competing financial interests.

Data Availability

The data that support the findings of this study are available from the corresponding authors upon reasonable request.

ORCID

Yizhan Xie https://orcid.org/0000-0003-4062-7740

References

1. M.-T. F. Rodrigues et al., "A materials perspective on Li-ion batteries at extreme temperatures." Nat. Energy, **2**, 17108 (2017).
2. Z. Cheng et al., "Early warning of thermal runaway for larger-format lithium iron-phosphate battery by coupling internal pressure and temperature." Appl. Energy, **383**, 125396 (2025).
3. X. Lai et al., "Enhancing early warning systems: Experimental investigation of physical signals in thermal runaway evolution of large-capacity lithium iron phosphate batteries." J. Power Sources, **632**, 236389 (2025).
4. T. M. Bandhauer, S. Garimella, and T. F. Fuller, "A critical review of thermal issues in lithium-ion batteries." J. Electrochem. Soc., **158**, R1 (2011).
5. L. Lu, X. Han, J. Li, J. Hua, and M. Ouyang, "A review on the key issues for lithium-ion battery management in electric vehicles." J. Power Sources, **226**, 272 (2013).
6. J. Huang et al., "Operando decoding of chemical and thermal events in commercial Na(Li)-ion cells via optical sensors." Nat. Energy, **5**, 674 (2020).
7. L. E. Downie and J. Dahn, "Determination of the voltage dependence of parasitic heat flow in lithium ion cells using isothermal microcalorimetry." J. Electrochem. Soc., **161**, A1782 (2014).
8. P. Desai, J. Huang, H. Hijazi, L. Zhang, S. Mariyappan, and J. Tarascon, "Deciphering interfacial reactions via optical sensing to tune the interphase chemistry for optimized Na-ion electrolyte formulation." Adv. Energy Mater., **11**, 2101490 (2021).
9. K. Maher and R. Yazami, "A study of lithium ion batteries cycle aging by thermodynamics techniques." J. Power Sources, **247**, 527 (2014).
10. J. Huang, C. Delacourt, P. Desai, and J.-M. Tarascon, "Operando entropy profiling of sodium-ion batteries via optical fiber sensing for thermal management and ageing monitoring." J. Electrochem. Soc., **171**, 030516 (2024).
11. J. Huang et al., "Unravelling thermal and enthalpy evolutions of commercial sodium-ion cells upon cycling ageing via fiber optic sensors." J. Electrochem. Soc., **170**, 090510 (2023).
12. J. Huang, S. T. Boles, and J.-M. Tarascon, "Sensing as the key to battery lifetime and sustainability." Nat Sustain, **5**, 194 (2022).
13. K. Li, L. Wang, Y. Wang, X. Feng, F. Jiang, and M. Ouyang, "Correlating phase transition with heat generation through calorimetric data." eScience, **4**, 100226 (2024).
14. J. Huang, L. A. Blanquer, C. Gervillié, and J.-M. Tarascon, "Distributed fiber optic sensing to assess in-live temperature imaging inside batteries: rayleigh and FBGs." J. Electrochem. Soc., **168**, 060520 (2021).
15. Y. Mao et al., "Evaluation of heat generation and thermal degradation of lithium ion batteries by a calorimetry method." J. Electrochem. Soc., **168**, 060553 (2021).
16. C. Lin, S. Xu, and J. Liu, "Measurement of heat generation in a 40 Ah $LiFePO_4$ prismatic battery using accelerating rate calorimetry." Int. J. Hydrogen Energy, **43**, 8375 (2018).
17. J. Deng et al., "Investigation of power battery heat generation measurement method with insulated cotton." J Energy Storage, **32**, 101807 (2020).
18. Y. Kobayashi, H. Miyashiro, K. Kumai, K. Takei, T. Iwahori, and I. Uchida, "Precise electrochemical calorimetry of $LiCoO_2$/graphite lithium-ion cell." J. Electrochem. Soc., **149**, A978 (2002).
19. L. Millet, M. Bruch, P. Raab, S. Lux, and M. Vetter, "Isothermal calorimeter heat measurements of a 20Ah lithium iron phosphate battery cell." *Twelfth International Conference on Ecological Vehicles and Renewable Energies (EVER)***2017**, 1 (2017), Twelfth International Conference on Ecological Vehicles and Renewable Energies (EVER) Monte-Carlo, Monaco IEEE.
20. S. Oh, S. Park, and K. Yoo, "Isothermal battery calorimetry analysis on a thermal behavior of Li-ion battery for electric vehicle." J. Energy Storage, **75**, 109678 (2024).
21. P. Rodríguez-Iturriaga, V. M. García, S. Rodríguez-Bolívar, E. E. Valdés, D. Anseán, and J. A. López-Villanueva, "A coupled electrothermal lithium-ion battery reduced-order model including heat generation due to solid diffusion." Appl. Energy, **367**, 123327 (2024).
22. X. Gao, K. Li, Y. Cao, G. J. Offer, and H. Wang, "Simulation and understanding of degraded lithium-ion battery self-heating ignition." Appl. Energy, **384**, 125435 (2025).
23. D. Bernardi, E. Pawlikowski, and J. Newman, "A general energy balance for battery systems." J. Electrochem. Soc., **132**, 5 (1985).
24. N. Nieto et al., "Thermal modeling of large format lithium-ion cells." J. Electrochem. Soc., **160**, A212 (2013).
25. C. Forgez, D. Vinh Do, G. Friedrich, M. Morcrette, and C. Delacourt, "Thermal modeling of a cylindrical $LiFePO_4$/graphite lithium-ion battery." J. Power Sources, **195**, 2961 (2010).
26. C.-H. Doh, Y.-C. Ha, and S. Eom, "Entropy measurement of a large format lithium ion battery and its application to calculate heat generation." Electrochim. Acta, **309**, 382 (2019).
27. R. Cao, X. Zhang, and H. Yang, "Prediction of the heat generation rate of lithium-ion batteries based on three machine learning algorithms." Batteries, **9**, 165 (2023).
28. H. Pang, L. Wu, J. Liu, X. Liu, and K. Liu, "Physics-informed neural network approach for heat generation rate estimation of lithium-ion battery under various driving conditions." J Energy Chem, **78**, 1 (2023).
29. S. Arora, W. Shen, and A. Kapoor, "Neural network based computational model for estimation of heat generation in $LiFePO_4$ pouch cells of different nominal capacities." Comput. Chem. Eng., **101**, 81 (2017).
30. S. Panchal, I. Dincer, M. Agelin-Chaab, R. Fraser, and M. Fowler, "Experimental and theoretical investigations of heat generation rates for a water cooled $LiFePO_4$ battery." Int J Heat Mass Transf, **101**, 1093 (2016).
31. D. Mahboubi, I. Jafari Gavzan, M. H. Saidi, and N. Ahmadi, "Developing an electro-thermal model to determine heat generation and thermal properties in a lithium-ion battery." J. Therm. Anal. Calorim., **147**, 12253 (2022).
32. N. Damay, C. Forgez, M.-P. Bichat, and G. Friedrich, "A method for the fast estimation of a battery entropy-variation high-resolution curve—Application on a commercial $LiFePO_4$/graphite cell." J. Power Sources, **332**, 149 (2016).
33. S. J. Bazinski and X. Wang, "Predicting heat generation in a lithium-ion pouch cell through thermography and the lumped capacitance model." J. Power Sources, **305**, 97 (2016).
34. H. Pang, L. Guo, L. Wu, J. Jin, F. Zhang, and K. Liu, "A novel extended Kalman filter-based battery internal and surface temperature estimation based on an improved electro-thermal model." J. Energy Storage, **41**, 102854 (2021).
35. X. Lin et al., "Online parameterization of lumped thermal dynamics in cylindrical lithium ion batteries for core temperature estimation and health monitoring." IEEE Trans Contr Syst Technol, **21**, 1745 (2013).
36. H. Dai, L. Zhu, J. Zhu, X. Wei, and Z. Sun, "Adaptive kalman filtering based internal temperature estimation with an equivalent electrical network thermal model for hard-cased batteries." J. Power Sources, **293**, 351 (2015).
37. Y. Inui, S. Hirayama, and T. Tanaka, "Detailed estimation method of heat generation during charge/discharge in lithium-ion battery using equivalent circuit." Electr. Commun. Jpn., **102**, 3 (2019).
38. X. Zhao, H. He, Z. Wei, R. Huang, H. Yue, and X. Guo, "Embedded fiber sensing-enabled multi state joint observation of smart lithium-ion battery based on distributed thermal modeling." J. Energy Storage, **118**, 116085 (2025).
39. P. Li, Z. Wei, K. Wu, J. Hu, Y. Yu, and H. He, "Embedded sensing-enabled distributed thermal modeling and nondestructive thermal monitoring of lithium-ion battery." IEEE T Transp. Electr., **10**, 7019 (2024).
40. G. Sidebotham, "Thermal circuits." Heat Transfer Modeling (Springer International Publishing, Switzerland)3 (2015).
41. J. Zhang, X.-G. Yang, F. Sun, Z. Wang, and C.-Y. Wang, "An online heat generation estimation method for lithium-ion batteries using dual-temperature measurements." Appl. Energy, **272**, 115262 (2020).

42. W. Yuan, Y. He, B. Li, J. Zhou, Z. Ma, and C. Li, "Improved cauer thermal network considering thermal coupling effects of multi-chip modules." *IET Power Electron.*, **13**, 3707 (2020).
43. T. Zhang, R. Tan, P. Zhu, T.-Y. Zhang, and J. Huang, "Unlocking ultrafast diagnosis of retired batteries via interpretable machine learning and optical fiber sensors." *ACS Energy Lett.*, **10**, 862 (2025).
44. Y. A. Çengel and A. J. Ghajar, "Heat conduction equation." *Heat Transfer a Practical Approach* (McGraw-Hill Higher Education, U.S.) 61 (2002), 2nd ed.
45. X. Feng, L. Lu, M. Ouyang, J. Li, and X. He, "A 3D thermal runaway propagation model for a large format lithium ion battery module." *Energy*, **115**, 194 (2016).
46. J. Qian and L. Sun, "Application of transfer function in predicting the temperature field of space equipment under periodic external heat flow." *Front Energy Res.*, **10**, 833071 (2022).
47. J. L. Basdevant, "The Padé approximation and its physical applications." *Fortschr. Phys.*, **20**, 283 (1972).
48. M. Vajta, "Some remarks on padé-approximations." *Proceedings of 3rd TEMPUS-INTCOM Symposium* (2000).
49. G. C. Goodwin et al., *Control System Design* vol. 240 (Prentice Hall Upper Saddle River) (2001).
50. P. Mellodge, "Introduction." *A Practical Approach to Dynamical Systems for Engineers* (Elsevier, Amsterdam) 1 (2016).
51. Calculus. Houston, *Calculus* (OpenStax, Rice University, Houston, Texas, USA) (2016).
52. Y. Liu et al., "Operando monitoring Lithium-ion battery temperature via implanting femtosecond-laser-inscribed optical fiber sensors." *Measurement*, **203**, 111961 (2022).
53. C. X. He et al., "A reduced-order thermal runaway network model for predicting thermal propagation of lithium-ion batteries in large-scale power systems." *Appl. Energy*, **373**, 123955 (2024).
54. R. R. Richardson, S. Zhao, and D. A. Howey, "On-board monitoring of 2-D spatially-resolved temperatures in cylindrical lithium-ion batteries: Part II. State estimation via impedance-based temperature sensing." *J. Power Sources*, **327**, 726 (2016).
55. R. Drummond, E. C. Tredenick, T. L. Kirk, M. Forghani, P. S. Grant, and S. Duncan, "Graded lithium-ion battery pouch cells to homogenise current distributions and reduce lithium plating." *J. Electrochem. Soc.*, **172**, 010518 (2025).
56. L. Xie et al., "A lithium-ion battery thermal management method based on silicon oil." *9th International Conference on Mechatronics and Robotics Engineering (ICMRE)* (IEEE, Piscataway, NJ) **2023**, 257 (2023).
57. J. Liu, S. Huang, and H. Chen, "Recent progress and prospects in oil-immersed battery thermal management system based on single-phase insulating oil: a review." *J. Therm. Anal. Calorim.*, **149**, 4263 (2024).
58. C. Wu et al., "A review on the liquid cooling thermal management system of lithium-ion batteries." *Appl. Energy*, **375**, 124173 (2024).
59. N. S. Nandagopal, Pe, "Convection heat transfer." *Fluid and thermal sciences* (Springer International Publishing, Switzerland) 205 (2022).
60. H. Wang et al., "Heat generation measurement and thermal management with phase change material based on heat flux for high specific energy power battery." *Appl. Therm. Eng.*, **194**, 117053 (2021).
61. J. N. Davidson, D. A. Stone, and M. P. Foster, "Required cauer network order for modelling of thermal transfer impedance." *Electron. Lett.*, **50**, 260 (2014).
62. P. Wang et al., "Real-time monitoring of internal temperature evolution of the lithium-ion coin cell battery during the charge and discharge process." *Extreme Mech. Let.t*, **9**, 459 (2016).
63. L. Matuck et al., "Towards smart and secure batteries: linking pressure and temperature profiles with electrochemical behavior through hybrid optical fiber sensors." *Chem. Eng. J.*, **500**, 156806 (2024).
64. J. Vetter et al., "Ageing mechanisms in lithium-ion batteries." *J. Power Sources*, **147**, 269 (2005).
65. P. Jindal, R. Katiyar, and J. Bhattacharya, "Evaluation of accuracy for bernardi equation in estimating heat generation rate for continuous and pulse-discharge protocols in LFP and NMC based Li-ion batteries." *Appl. Therm. Eng.*, **201**, 117794 (2022).